

Kohn-Luttinger Mechanism of Superconductivity in Twisted Bilayer WSe₂: Gate-Tunable Unconventional Pairing Symmetry

Wei Qin,^{1,*} Wen-Xuan Qiu,² and Fengcheng Wu^{2,†}

¹*Department of Physics, University of Science and Technology of China, Hefei, Anhui 230026, China*

²*School of Physics and Technology, Wuhan University, Wuhan 430072, China*

(Dated: September 25, 2024)

Motivated by the recent discovery of superconductivity in twisted bilayer WSe₂, we theoretically investigate the pairing instability induced by Coulomb interaction via the Kohn-Luttinger mechanism. Within random phase approximation, we show that the Coulomb repulsion is strongly screened around the morié length scale, resulting in attractive regimes that facilitate electron pairing in unconventional channels. By solving the linearized gap equation, we find that the maxima of the superconducting critical temperature occur at the van Hove singularities in the density of states, with magnitude on the order of ~ 0.2 K, comparable with experimental observations. Moreover, we identify a phase transition from an *f*-wave-like pairing state to a doubly degenerate *d*-wave-like pairing state upon increasing the electric displacement field. These findings provide a purely electronic explanation of the superconducting state observed in twisted bilayer WSe₂, offering insights into the interplay between superconductivity and other correlated states in twisted transition metal dichalcogenides.

Introduction.—The discovery of superconductivity and correlated insulating states in magic-angle twisted bilayer graphene [1, 2] has stimulated extensive studies on the morié superlattices [3–18], resulting in the observation of a plethora of intriguing strongly correlated phenomena. Beyond graphene-based moiré systems, twisted transition metal dichalcogenides (tTMDs) have emerged as another prominent and widely studied class of moiré materials [19–23]. Monolayer TMDs are semiconductors with strong Ising-type spin-orbit coupling [24], characterized by spin-valley locking effect in the low-energy bands. By stacking two layers of TMD materials together, a lattice mismatch or small twist angle between them can generate a morié superlattice, leading to the formation of morié flat bands that strongly enhance the electronic correlation effects [19–21], giving rise to phenomena such as Mott insulators [25–27], magnetism [28–30], generalized Wigner crystals [25, 31, 32], and heavy fermions [33]. The combination of strong correlation and non-trivial band topology has further led to the emergence of integer and fractional Chern insulators [34–41], as well as the fractional quantum spin Hall insulator [42]. Although a wide range of correlated phenomena has been observed in both graphene- and TMD-based moiré systems, robust evidence for superconductivity has been conclusively established only in the former.

Recently, robust superconductivity has been reported in tWSe₂ at two distinct twist angles: $\theta = 3.65^\circ$ [43] and $\theta = 5^\circ$ [44]. In the former case, superconductivity is observed at filling factor $\nu = -1$ (one hole per morié unit cell) under minimal displacement fields, with an optimal critical temperature T_c of 0.22 K. The superconducting phase is in proximity to a correlated insulator phase at the same ν but finite displacement fields. By contrast, no prominent correlated insulator is observed at $\theta = 5^\circ$, where the superconducting state emerges around

the van Hove singularity with an optimal T_c of 0.4 K under large displacement fields. In addition, the superconducting phase is adjacent to a metallic phase with enhanced resistivity attributed to Fermi surface (FS) reconstruction [44]. Although several models have been examined in relation to superconductivity in this system [45–52], the microscopic pairing mechanism remains far from definitive.

In this Letter, we investigate the mechanism for superconductivity induced solely by long-range Coulomb interaction in tWSe₂. Using the continuum band structure model with realistic material parameters [21, 53], we find the repulsive Coulomb interaction is strongly screened around the morié length scale, resulting in attractive regimes that lead to pairing instability. The real-space structures of the screened Coulomb potential are nearly independent of the electric displacement field. Based on the screened Coulomb potential, we solve the linearized gap equation for superconductivity and find that the T_c maxima occur at the van Hove singularities (VHSs) for given displacement fields, with an optimal value of ~ 0.2 K, which is comparable to experimentally reported values [43, 44]. In particular, by increasing the displacement field, our calculations reveal a first order phase transition from *f*-wave-like pairing symmetry to doubly degenerate *d*-wave-like pairing symmetry. The values of T_c in both phases are enhanced (reduced) upon decreasing (increasing) the environmental dielectric constant.

Model.—The low-energy band structure of tWSe₂ is described by the continuum model [21], with the two valleys connected by time-reversal symmetry. The *K*-valley-project Hamiltonian

$$\mathcal{H}_K = \begin{pmatrix} h_+(\mathbf{k}) + U_+(\mathbf{r}) & T(\mathbf{r}) \\ T^\dagger(\mathbf{r}) & h_-(\mathbf{k}) + U_-(\mathbf{r}) \end{pmatrix}, \quad (1)$$

where $h_\pm(\mathbf{k}) = -\hbar^2(\mathbf{k} - \boldsymbol{\kappa}_\pm)^2/2m^*$ are the effective mass

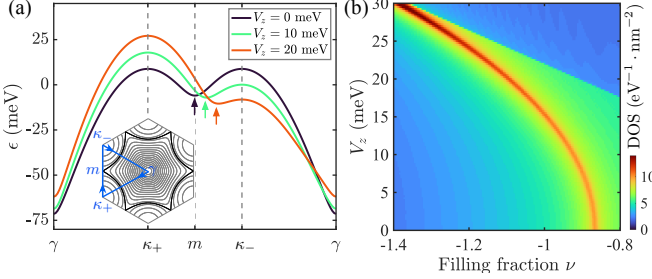


FIG. 1. (a) The K -valley first morié band along high-symmetry lines of the MBZ, where the vertical arrows mark the saddle points. The inset shows the energy contours for $V_z = 0$ meV, with the bolded curve highlighting the FS at van Hove filling. (b) DOS versus hole filling fraction ν and layer potential V_z .

($m^* = 0.43m_0$) approximation of the kinetic energies for the top and bottom WSe₂ with m_0 being the bare electron mass, and κ_{\pm} denote the corners of the moiré Brillouin zone (MBZ). The intra- and inter-layer morié potentials are given by

$$U_{\pm}(\mathbf{r}) = 2V \sum_{j=1,3,5} \cos(\mathbf{G}_j \cdot \mathbf{r} \pm \psi) \pm V_z, \quad (2)$$

$$T(\mathbf{r}) = w(1 + e^{-i\mathbf{G}_2 \cdot \mathbf{r}} + e^{-i\mathbf{G}_3 \cdot \mathbf{r}}),$$

where \mathbf{G}_j is the morié reciprocal lattice vector given by rotating $\mathbf{G}_1 = (4\pi\theta/\sqrt{3}a_0, 0)$ counterclockwisely with angle $(j-1)\pi/3$, $a_0 = 3.317$ Å is the lattice constant of monolayer WSe₂, and V_z denotes the layer potential induced by externally applied displacement field. In this study, we choose model parameters $(V, \psi, w) = (9.0 \text{ meV}, 128^\circ, 18 \text{ meV})$ obtained from fitting first-principles calculations [53].

Figure 1(a) shows the first morié band in K valley for $\theta = 5^\circ$ at three typical values of V_z , revealing a bandwidth of approximately 80 meV. For $V_z = 0$ meV, saddle points are found at the m points of the MBZ depicted in the inset. As V_z increases, these saddle points shift away from the m point towards the κ_- point, as marked by the vertical arrows in Fig. 1(a). As shown in Fig. 1(b), band structures around the saddle points give rise to VHSs in the density of states (DOS). By increasing V_z , the VHS moves to higher hole fillings with enhanced magnitude.

The bare form of Coulomb interaction in the plane-wave basis is given as

$$H_c = \frac{1}{2A} \sum_{\mathbf{q}} V_0(\mathbf{q}) \hat{\rho}_{\mathbf{q}} \hat{\rho}_{-\mathbf{q}}, \quad (3)$$

where A denotes the area of the system, $V_0(\mathbf{q}) = (2\pi e^2/\epsilon q) \tanh(qd_s)$ is the Coulomb potential screened by dual metallic gates placed at a distance d_s away from the tWSe₂, $\hat{\rho}_{\mathbf{q}} = \sum_{\mathbf{k}\tau} c_{\mathbf{k}\tau}^\dagger c_{\mathbf{k}+\mathbf{q}\tau}$ represents the electron density operator, and $c_{\mathbf{k}\tau}^\dagger$ ($c_{\mathbf{k}\tau}$) is the electron creation

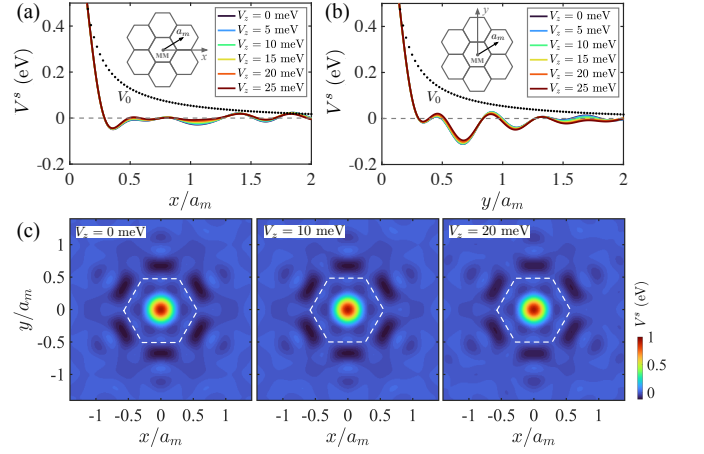


FIG. 2. (a)-(b) The real-space screened V^s (solid curves) and bare V_0 (dots) Coulomb potentials plotted along (a) x and (b) y directions, where $a_m = a_0/\theta$ denotes the morié period, as defined in the inset. (c) 2D color maps of $V^s(\mathbf{r})$ for three typical values of V_z , where the dashed hexagons indicate the morié supercell. The coordinate origins in these plots are set at the MM stacking center of tWSe₂. These results are obtained at the van Hove fillings for temperature $T = 50$ mK.

(annihilation) operator at valley τ and wavevector \mathbf{k} . Unless otherwise specified, we choose $\theta = 5^\circ$, $\epsilon = 5$, and $d_s = 11$ nm in the following calculations to account for the twist angle, dielectric constant, and thickness of the hBN spacer layers, aligning with experimental conditions in Ref. 44.

Screened Coulomb interaction.—We explore the Kohn-Luttinger mechanism [58] of pairing instability induced by long-range Coulomb interactions that are screened by particle-hole fluctuations. Within the random phase approximation (RPA) [54, 55], the effective electron-electron interaction

$$\Pi_{\mathbf{Q}, \mathbf{Q}'}(\mathbf{q}) = V_0(\mathbf{q} + \mathbf{Q}) [1 + \sum_{\mathbf{Q}''} \Pi_{\mathbf{Q}, \mathbf{Q}''}(\mathbf{q}) V_{\mathbf{Q}'', \mathbf{Q}'}^s(\mathbf{q})], \quad (4)$$

where \mathbf{Q}' 's are morié reciprocal lattice vectors and \mathbf{q} is the wavevector defined within the MBZ. A compact matrix form of the above equation is $V^s = V_0 / (\mathbb{1} - \Pi V_0)$. The static charge polarization function reads [56]

$$\Pi_{\mathbf{Q}, \mathbf{Q}'}(\mathbf{q}) = \frac{1}{A} \sum_{mm' \mathbf{k}} \frac{f(\epsilon_{m\mathbf{k}}) - f(\epsilon_{m'\mathbf{k}+\mathbf{q}})}{\epsilon_{m\mathbf{k}} - \epsilon_{m'\mathbf{k}+\mathbf{q}}} \sum_{l' \mathbf{G} \mathbf{G}'} [\rho_{m\mathbf{k}}]_{l, \mathbf{G}; l', \mathbf{G}'} [\rho_{m'\mathbf{k}+\mathbf{q}}]_{l', \mathbf{G}'+\mathbf{Q}'; l, \mathbf{G}+\mathbf{Q}} \quad (5)$$

where $\epsilon_{m\mathbf{k}}$ denotes the electron energy of morié band index m at wavevector \mathbf{k} , $f(\epsilon)$ is the Fermi-Dirac distribution function, \mathbf{G}' 's are morié reciprocal lattice vectors, l is the layer index, and the density matrix $\rho_{m\mathbf{k}} = |m\mathbf{k}\rangle \langle m\mathbf{k}|$ with $|m\mathbf{k}\rangle$ being the corresponding wave function. Here $\Pi(\mathbf{q})$ in Eq. (5) denotes the total polarization function with an implicit summation over the valley index. At

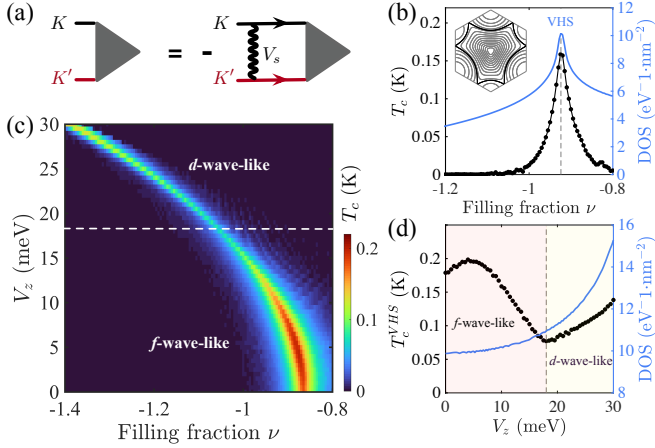


FIG. 3. (a) Diagrammatic representation of the linearized gap equation, where the bolded wave line and filled triangle denote the screened Coulomb interaction and superconducting order parameter, respectively. (b) Critical temperature T_c (black dots) and DOS (blue curve) versus filling fraction ν for $V_z = 10$ meV. The inset depicts the energy contours, with FS at the VHS highlighted by the bolded curve. (c) 2D map of T_c versus ν and V_z , where the dashed line indicates the phase boundary between f -wave-like and d -wave-like pairing states. (d) T_c^{VHS} (black dots) and DOS (blue curve) at the VHSs for different values of V_z .

low temperatures, the leading contribution to $\Pi(\mathbf{q})$ are from the electronic states around the FS. Therefore, in the following calculations, we adopt the single-band approximation by keeping only the contributions from the first morié band.

Figures 2(a)-(b) show the real-space screened Coulomb potential $V^s(\mathbf{r})$ measured from the MM stacking center of tWSe₂ [56], exhibiting a significant reduction around the morié length scale. Unlike the bare Coulomb potential, which is always repulsive, $V^s(\mathbf{r})$ develops attractive regimes that may lead to pairing instability of the system. For $V_z = 0$ meV, the two-dimensional (2D) map of $V^s(\mathbf{r})$ depicted in Fig. 2(c) possesses six-fold rotational symmetry and is characterized by six prominent attractive regimes near the edges of the morié Wigner-Seitz cell. As V_z increases, the key structure of $V^s(\mathbf{r})$ remains nearly unaffected, with only a slight reduction in magnitude attributed to the enhanced DOS. The results of $V^s(\mathbf{r})$ measured from the MX and XM stacking centers are provided in the SM [56], where similar real-space structures are revealed.

Superconductivity.—Based on the RPA effective interaction, the superconducting critical temperature T_c and pairing symmetry are determined by solving the linearized gap equation, as schematically depicted in Fig. 3(a). In this study, we focus on electron pairing from opposite valleys because it is energetically more favorable in the presence of electric displacement fields. We solve the linearized gap equation in the band representation

[56], wherein Fig. 3(a) is interpreted as

$$\Delta_{\mathbf{k}} = -\frac{1}{A} \sum_{\mathbf{k}'} V_b^s(\mathbf{k}, \mathbf{k}') \frac{\tanh(\beta \epsilon_{\mathbf{k}'}/2)}{2\epsilon_{\mathbf{k}'}} \Delta_{\mathbf{k}'} . \quad (6)$$

Here $\Delta_{\mathbf{k}}$ denotes the order parameter, $\beta = 1/k_B T$ with k_B being the Boltzmann constant, and $\epsilon_{\mathbf{k}'}$ is the first morié band energy measured from the Fermi level. In Eq. (6), V_b^s represents the screened Coulomb potential projected onto the first morié band and is given by [56]

$$V_b^s(\mathbf{k}, \mathbf{k}') = \sum_{\mathbf{Q}\mathbf{Q}'} V_{\mathbf{Q}, \mathbf{Q}'}^s(\mathbf{k} - \mathbf{k}') \sum_{l' l' \mathbf{G} \mathbf{G}'} [\rho_{\mathbf{k}}]_{l, \mathbf{G}; l', \mathbf{G}'} [\rho_{\mathbf{k}'}]_{l', \mathbf{G}' - \mathbf{Q}'; l, \mathbf{G} - \mathbf{Q}} . \quad (7)$$

The T_c is given by equaling the largest eigenvalue of Eq. (6) to 1, with the pairing symmetry encoded in the eigenvector(s). As detailed in the SM [56], a "two-step" discretization scheme is employed in the numerical solution of Eq. (6), yielding smooth variations of T_c to within few millikelvins.

Figure 3(b) shows the dependence of T_c on ν for a fixed value of $V_z = 10$ meV. The behavior of T_c follows the trend of the DOS, exhibiting a cusp at the VHS, which arises from the saddle-like band structure depicted in the inset of Fig. 3(b). These characters are indicative of superconductivity in the weak-coupling limit. A 2D map of T_c is depicted in Fig. 3(c), obtained by systematically varying both the ν and V_z . By comparing Figs. 3(c) and 1(b), we find the T_c maxima consistently occur at the VHSs for given values of V_z . Remarkably, optimal superconductivity is found at the VHS for a finite value of $V_z = 5$ meV, yielding a critical temperature $T_c \sim 0.2$ K, which is consistent with the experimentally reported value of 0.4 K [44]. Figure 3(d) plots the T_c^{VHS} and the corresponding DOS at VHSs for different values of V_z . In contrast to the DOS, which increases monotonously with increasing V_z , T_c^{VHS} does not follow this trend and exhibits an intriguing non-monotonic behavior. Specifically, as V_z increases from 0 meV, T_c^{VHS} initially rises to a maximum at $V_z = 5$ meV, subsequently decreases to a minimum at $V_z = 18$ meV, and then increases again. The increase in T_c from $V_z = 0$ to 5 meV is attributed to the enhancement of the DOS, while the emergence of a minimum in T_c at $V_z = 18$ meV is found to be associated with a first-order phase transition, as elaborated below.

Pairing symmetry.—To gain further insights into superconductivity illustrated in Fig. 3(c), we examine $\Delta_{\mathbf{k}}$ at the VHSs for two typical values of V_z . As shown in Fig. 4(a), $\Delta_{\mathbf{k}}$ of the leading pairing channel for $V_z = 10$ meV exhibits a three-fold rotational symmetry. The extracted values of $\Delta_{\mathbf{k}}$ along the FS are denoted by $\Delta(\phi)$ and are plotted in Fig. 4(b). Six nodes (zeros) of $\Delta(\phi)$ are found in the range $\phi \in [-\pi, \pi]$, indicating an f -wave-like pairing symmetry. To quantify the analysis, we perform

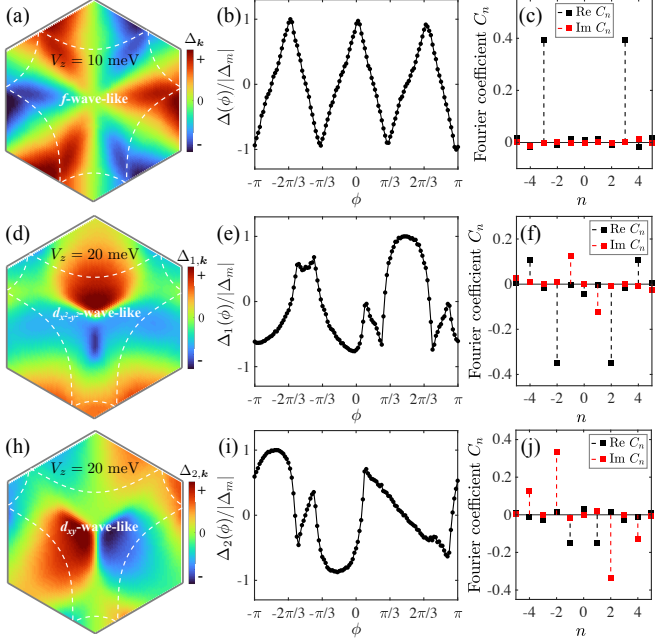


FIG. 4. (a) The k -space superconducting order parameter $\Delta_{\mathbf{k}}$ for $V_z = 10$ meV at van Hove filling, where the dashed (white) curve denotes the FS. (b) Samplings of $\Delta_{\mathbf{k}}$ along the FS at equally spaced angles ϕ relative to the MBZ center. Here $\Delta(\phi)$ is normalized to its maximum value Δ_m . (c) Fourier coefficients C_n of $\Delta(\phi)$, with integer n labeling different angular momentum channels. (d),(h) k -space structures of the doubly degenerate order parameters for $V_z = 20$ meV, where the dashed (white) line delineates the FS at van Hove filling. (e),(i) Samplings of $\Delta_{1,\mathbf{k}}$ and $\Delta_{2,\mathbf{k}}$ along the FS, respectively. (f),(j) Fourier decompositions of $\Delta_1(\phi)$ and $\Delta_2(\phi)$ shown in (e) and (i).

the Fourier decomposition

$$\Delta(\phi) = \sum_n C_n e^{in\phi}, \quad (8)$$

where C_n denotes the Fourier coefficient of angular momentum channel n . As shown in Fig. 4(c), the f -wave channel with $n = \pm 3$ predominates in the contribution to $\Delta(\phi)$, indicating that $\Delta(\phi) \propto \cos(3\phi)$.

For $V_z = 20$ meV, the leading pairing instability is doubly degenerate, characterized by two orthogonal order parameters, $\Delta_{1,\mathbf{k}}$ and $\Delta_{2,\mathbf{k}}$, as depicted in Figs. 4(d) and (h), respectively. The extracted values $\Delta_{1,2}(\phi)$ along FS are plotted in Figs. 4(e) and (i), showing otherwise intricate structures. By performing Fourier decomposition, we find that the dominant contributions to $\Delta_{1,2}(\phi)$ arise from the d -wave channel with $n = \pm 2$, as illustrated in Figs. 4(f) and (j). Moreover, the d -wave channel co-exists with the p -wave ($n = \pm 1$) and g -wave ($n = \pm 4$) channels, resulting in the following approximations

$$\begin{aligned} \Delta_1(\phi) &\propto |C_1| \sin \phi + |C_2| \cos 2\phi + |C_4| \cos 4\phi \\ \Delta_2(\phi) &\propto |C_1| \cos \phi + |C_2| \sin 2\phi + |C_4| \sin 4\phi, \end{aligned} \quad (9)$$

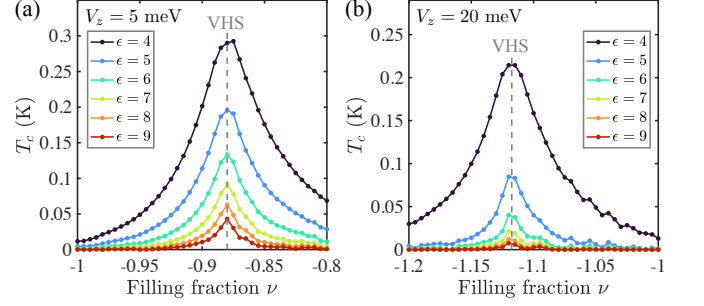


FIG. 5. (a)-(b) The critical temperature T_c versus ν and dielectric constant ϵ for (a) $V_z = 5$ meV and (b) $V_z = 20$ meV, where the dashed lines indicates the corresponding van Hove fillings. The pairing symmetry is f - and d -wave-like in (a) and (b), respectively.

with $(|C_1|, |C_2|, |C_4|) \approx (0.14, 0.35, 0.12)$. This result also implies that $\Delta_{1,2}$ are predominantly characterized by $d_{x^2-y^2}$ and d_{xy} symmetries, respectively, as marked in Figs. 4(d) and (h).

We further examine the impact of varying dielectric constant ϵ on T_c for the f - and d -wave-like pairing symmetries at V_z of 5 meV and 20 meV, respectively. As shown in Fig. 5, increasing (decreasing) of ϵ leads to an reduction (enhancement) of T_c for both pairing symmetries. These results may be validated by future experiments, providing evidence for a purely electronic pairing mechanism.

Symmetry analysis.—In the absence of the displacement field, the continuum model of tWSe₂ exhibits an emergent \hat{D}_{3d} point group symmetry [21]. The f -wave-like pairing state observed at $V_z = 0$ meV belongs to the 1D odd-parity A_{1u} irreducible representation. The presence of a displacement field has two notable effects. First, as illustrated in Fig. 1(b), it increases the DOS, thereby promoting superconductivity. Secondly, it breaks the emergent inversion symmetry of the continuum model [57], leading to the mixing between the odd-parity A_{1u} and even-parity A_{1g} irreducible representations, which in turn weakens the f -wave-like pairing state. The competition between the two effects results in the dome-like behavior of T_c in $V_z \in (0, 18)$ meV, as illustrated in Fig. 3(d). For sufficiently large displacement fields, the doubly degenerate states belonging to the 2D E representation of \hat{C}_3 point group predominate, and the T_c is enhanced upon further increasing V_z due to the increased DOS. Generally, the eigenvectors of E representation comprise mixtures of (p_x, p_y) , $(d_{x^2-y^2}, d_{xy})$, and higher order terms because $e^{in\phi}$ and $e^{i(n+3)\phi}$ are indistinguishable within \hat{C}_3 point group symmetry. The precise mixing coefficients among p -, d -, and g -wave channels depend on the specific band structure. In this work, we identify the dominant pairing symmetry associated with the E representation as d -wave pairing, justifying the term “ d -wave-like” used in the preceding discussions.

Discussion.—The present study provides a purely electronic mechanism for the superconductivity observed recently in tWSe₂ [43, 44]. For $\theta = 5^\circ$, the theoretically predicted optimal superconductivity occurs at the VHS under a finite displacement field, with $T_c \sim 0.2$ K. These characters align closely with experimental observations in $\theta = 5^\circ$ sample [44]. Moreover, we predict a phase transition from *f*-wave-like to doubly degenerate *d*-wave-like pairing states with increasing the displacement field. By reducing the temperature below T_c , the latter can further form either chiral $d \pm id$ or nematic pairing states. In the weak-coupling limit, the most likely pairing state is the $d \pm id$ state [59, 60], which leads to the spontaneous breaking of time-reversal symmetry.

The present theory does fall short in explaining certain precise aspects, such as the experimental observation that superconductivity emerges within a narrow regime near the VHS at $\nu = -1$ [44]. This discrepancy may arise from some limitations of the RPA calculation. For instance, this theory does not incorporate interaction-induced band renormalization, which could modify the phase diagram shown in Fig. 3(c). Moreover, the RPA disregards the exchange enhancement effect, which could lead to pronounced quantum fluctuations, provided that the FSs from the two valleys are strongly nested [60]. The Ising-type spin-orbit coupling in WSe₂ converts the inter-valley fluctuation into the antiferromagnetic type, which may mediate superconductivity and thereby explain the proximity between the superconducting and correlated metallic phases observed in experiments [44]. For smaller θ , the electronic correlations are dramatically enhanced, as evidenced by the emergence of correlated insulator states [25–27, 43], rendering reliance on RPA-level calculations invalid. As detailed in the SM [56], although our calculated values of T_c are comparable to experimental values for $\theta = 3.65^\circ$ [43], the theoretical phase diagram deviates from the experimental one.

In summary, our theory is more suitable for tWSe₂ with larger twist angles, such as $\theta = 5^\circ$, where we predict a phase transition from *f*-wave-like to *d*-wave-like pairing states, controlled by the electric gate. A comprehensive study of different types of the correlated phase in tWSe₂ on an equal footing could be performed through, for example, functional renormalization group calculations, which calls for further study.

Acknowledgement.—This work is supported by National Natural Science Foundation of China (Grant Nos.12474134 and 1227433)

Note added.—During the preparation of this manuscript, we became aware of a related preprint posted on arxiv [61].

[†] wufcheng@whu.edu.cn

- [1] Y. Cao, V. Fatemi, S. Fang, K. Watanabe, T. Taniguchi, E. Kaxiras, and P. Jarillo-Herrero, Unconventional superconductivity in magic-angle graphene superlattices, *Nature (London)* **556**, 43 (2018).
- [2] Y. Cao, V. Fatemi, A. Demir, S. Fang, S. L. Tomarken, J. Y. Luo, J. D. Sanchez-Yamagishi, K. Watanabe, T. Taniguchi, E. Kaxiras, R. C. Ashoori, and P. Jarillo-Herrero, Correlated insulator behaviour at half-filling in magic-angle graphene superlattices, *Nature (London)* **556**, 80 (2018).
- [3] M. Yankowitz, S. Chen, H. Polshyn, Y. Zhang, K. Watanabe, T. Taniguchi, D. Graf, A. F. Young, and C. R. Dean, Tuning superconductivity in twisted bilayer graphene, *Science* **363**, 1059 (2019).
- [4] X. Lu, P. Stepanov, W. Yang, M. Xie, M. A. Aamir, I. Das, C. Urgell, K. Watanabe, T. Taniguchi, G. Zhang, A. Bachtold, A. H. MacDonald, and D. K. Efetov, Superconductors, orbital magnets and correlated states in magic-angle bilayer graphene, *Nature (London)* **574**, 653 (2019).
- [5] L. Balents, C. R. Dean, D. K. Efetov, and A. F. Young, Superconductivity and strong correlations in moiré flat bands, *Nat. Phys.* **16**, 725 (2020).
- [6] P. Stepanov, I. Das, X. Lu, A. Fahimniya, K. Watanabe, T. Taniguchi, F. H. L. Koppens, J. Lischner, L. Levitov, and D. K. Efetov, Untying the insulating and superconducting orders in magic-angle graphene, *Nature (London)* **583**, 375 (2020).
- [7] Y. Saito, J. Ge, K. Watanabe, T. Taniguchi, and A. F. Young, Independent superconductors and correlated insulators in twisted bilayer graphene, *Nat. Phys.* **16**, 926 (2020).
- [8] D. Wong, K. P. Nuckolls, M. Oh, B. Lian, Y. Xie, S. Jeon, K. Watanabe, T. Taniguchi, B. A. Bernevig, and A. Yazdani, Cascade of electronic transitions in magic-angle twisted bilayer graphene, *Nature (London)* **582**, 198 (2020).
- [9] U. Zondiner, A. Rozen, D. Rodan-Legrain, Y. Cao, R. Queiroz, T. Taniguchi, K. Watanabe, Y. Oreg, F. von Oppen, A. Stern, E. Berg, P. Jarillo-Herrero, and S. Ilani, Cascade of phase transitions and Dirac revivals in magic-angle graphene, *Nature (London)* **582**, 203 (2020).
- [10] X. Liu, Z. Wang, K. Watanabe, T. Taniguchi, O. Vafek, and J. I. A. Li, Tuning electron correlation in magic-angle twisted bilayer graphene using Coulomb screening, *Science* **371**, 1261 (2021).
- [11] J. M. Park, Y. Cao, K. Watanabe, T. Taniguchi, and P. Jarillo-Herrero, Tunable strongly coupled superconductivity in magic-angle twisted trilayer graphene, *Nature (London)* **590**, 249 (2021).
- [12] Z. Hao, A. M. Zimmerman, P. Ledwith, E. Khalaf, D. H. Najafabadi, K. Watanabe, T. Taniguchi, A. Vishwanath, and P. Kim, Electric field-tunable superconductivity in alternating-twist magic-angle trilayer graphene, *Science* **371**, 1133 (2021).
- [13] P. Stepanov, M. Xie, T. Taniguchi, K. Watanabe, X. Lu, A. H. MacDonald, B. A. Bernevig, and D. K. Efetov, Competing zero-field Chern insulators in superconducting twisted bilayer graphene, *Phys. Rev. Lett.* **127**, 197701 (2021).
- [14] Y. Saito, F. Yang, J. Ge, X. Liu, T. Taniguchi, K. Watanabe, J. I. A. Li, E. Berg, and A. F. Young, Isospin pomeranchuk effect in twisted bilayer graphene, *Nature (London)*

* qinwei5@ustc.edu.cn

- don) **592**, 220 (2021).
- [15] Y. Cao, J. M. Park, K. Watanabe, T. Taniguchi, and P. Jarillo-Herrero, Large Pauli limit violation and reentrant superconductivity in magic-angle twisted trilayer graphene, arXiv:2103.12083 (2021).
- [16] Y. Choi, H. Kim, Y. Peng, A. Thomson, C. Lewandowski, R. Polski, Y. Zhang, H. S. Arora, K. Watanabe, T. Taniguchi, J. Alicea, and S. Nadj-Perge, Correlation driven topological phases in magic-angle twisted bilayer graphene, *Nature (London)* **589**, 536 (2021).
- [17] Y. Choi, H. Kim, C. Lewandowski, Y. Peng, A. Thomson, R. Polski, Y. Zhang, K. Watanabe, T. Taniguchi, J. Alicea, and S. Nadj-Perge, Interaction-driven band flattening and correlated phases in twisted bilayer graphene, *Nat. Phys.* **17**, 1375 (2021).
- [18] A. Jaoui, I. Das, G. D. Battista, J. Díez-Mérida, X. Lu, K. Watanabe, T. Taniguchi, H. Ishizuka, L. Levitov, D. K. Efetov, Quantum critical behaviour in magic-angle twisted bilayer graphene, arXiv:2108.07753 (2022).
- [19] F. Wu, T. Lovorn, E. Tutuc, and A. H. MacDonald, Hubbard Model Physics in Transition Metal Dichalcogenide Moiré Bands, *Phys. Rev. Lett.* **121**, 026402 (2018).
- [20] M. H. Naik and M. Jain, Ultraflatbands and Shear Solitons in Moiré Patterns of Twisted Bilayer Transition Metal Dichalcogenides, *Phys. Rev. Lett.* **121**, 266401 (2018).
- [21] F. Wu, T. Lovorn, E. Tutuc, I. Martin, and A. H. MacDonald, Topological Insulators in Twisted Transition Metal Dichalcogenide Homobilayers, *Phys. Rev. Lett.* **122**, 086402 (2019).
- [22] D. A. Ruiz-Tijerina and V. I. Fal'ko, Interlayer hybridization and moiré superlattice minibands for electrons and excitons in heterobilayers of transition-metal dichalcogenides, *Phys. Rev. B* **99**, 125424 (2019).
- [23] C. Schrade and L. Fu, Spin-valley density wave in moiré materials, *Phys. Rev. B* **100**, 035413 (2019).
- [24] D. Xiao, G.-B. Liu, W. Feng, X. Xu, and W. Yao, Coupled Spin and Valley Physics in Monolayers of MoS₂ and Other Group-VI Dichalcogenides, *Phys. Rev. Lett.* **108**, 196802 (2012).
- [25] E. C. Regan, D. Wang, C. Jin, M. I. Bakti Utama, B. Gao, X. Wei, S. Zhao, W. Zhao, Z. Zhang, K. Yumigeta, M. Blei, J. D. Carlström, K. Watanabe, T. Taniguchi, S. Tongay, M. Crommie, A. Zettl, and F. Wang, Mott and generalized Wigner crystal states in WSe₂/WS₂ moiré superlattices, *Nature (London)* **579**, 359 (2020).
- [26] Y. Tang, L. Li, T. Li, Y. Xu, S. Liu, K. Barmak, K. Watanabe, T. Taniguchi, A. H. MacDonald, J. Shan, and K. F. Mak, Simulation of Hubbard model physics in WSe₂/WS₂ moiré superlattices, *Nature (London)* **579**, 353 (2020).
- [27] L. Wang, E.-M. Shih, A. Ghiotto, L. Xian, D. A. Rhodes, C. Tan, M. Claassen, D. M. Kennes, Y. Bai, B. Kim, K. Watanabe, T. Taniguchi, X. Zhu, J. Hone, A. Rubio, A. N. Pasupathy, and C. R. Dean, Correlated electronic phases in twisted bilayer transition metal dichalcogenides, *Nat. Mater.* **19**, 861 (2020).
- [28] Y. Xu, K. Kang, K. Watanabe, T. Taniguchi, K. F. Mak, and J. Shan, A tunable bilayer Hubbard model in twisted WSe₂, *Nat. Nanotechnol.* **17**, 934 (2022).
- [29] E. Anderson, F.-R. Fan, J. Cai, W. Holtzmann, T. Taniguchi, K. Watanabe, D. Xiao, W. Yao, and X. Xu, Programming correlated magnetic states with gate-controlled moiré geometry, *Science* **381**, 325 (2023).
- [30] A. Ghiotto, L. Wei, L. Song, J. Zang, A. B. Tazi, D. Ostrom, K. Watanabe, T. Taniguchi, J. C. Hone, D. A. Rhodes, A. J. Millis, C. R. Dean, L. Wang, and A. N. Pasupathy, Stoner instabilities and Ising excitonic states in twisted transition metal dichalcogenides, arXiv:2405.17316 (2024).
- [31] Y. Xu, S. Liu, D. A. Rhodes, K. Watanabe, T. Taniguchi, J. Hone, V. Elser, K. F. Mak, and J. Shan, Correlated insulating states at fractional fillings of moiré superlattices, *Nature (London)* **587**, 214 (2020).
- [32] H. Li, S. Li, E. C. Regan, D. Wang, W. Zhao, S. Kahn, K. Yumigeta, M. Blei, T. Taniguchi, K. Watanabe, S. Tongay, A. Zettl, M. F. Crommie, and F. Wang, Imaging two-dimensional generalized Wigner crystals, *Nature (London)* **597**, 650 (2021).
- [33] W. Zhao, B. Shen, Z. Tao, Z. Han, K. Kang, K. Watanabe, T. Taniguchi, K. F. Mak, and J. Shan, Gate-tunable heavy fermions in a moiré Kondo lattice, *Nature (London)* **616**, 61 (2023).
- [34] T. Li, S. Jiang, B. Shen, Y. Zhang, L. Li, Z. Tao, T. Devakul, K. Watanabe, T. Taniguchi, L. Fu, J. Shan, and K. F. Mak, Quantum anomalous Hall effect from intertwined moiré bands, *Nature (London)* **600**, 641 (2021).
- [35] M. Bélanger, J. Fournier, and D. Sénecha, Superconductivity in the twisted bilayer transition metal dichalcogenide WSe₂: A quantum cluster study, *Phys. Rev. B* **106**, 235135 (2022).
- [36] V. Crépel, D. Guerci, J. Cano, J. H. Pixley, and A. Millis, Topological Superconductivity in Doped Magnetic Moiré Semiconductors, *Phys. Rev. Lett.* **131**, 056001 (2023).
- [37] J. Cai, E. Anderson, C. Wang, X. Zhang, X. Liu, W. Holtzmann, Y. Zhang, F. Fan, T. Taniguchi, K. Watanabe, Y. Ran, T. Cao, L. Fu, D. Xiao, W. Yao, and X. Xu, Signatures of fractional quantum anomalous Hall states in twisted MoTe₂, *Nature (London)* **622**, 63 (2023).
- [38] Y. Zeng, Z. Xia, K. Kang, J. Zhu, P. Knüppel, C. Vaswani, K. Watanabe, T. Taniguchi, K. F. Mak, and J. Shan, Thermodynamic evidence of fractional Chern insulator in moiré MoTe₂, *Nature (London)* **622**, 69 (2023).
- [39] H. Park, J. Cai, E. Anderson, Y. Zhang, J. Zhu, X. Liu, C. Wang, W. Holtzmann, C. Hu, Z. Liu, T. Taniguchi, K. Watanabe, J.-H. Chu, T. Cao, L. Fu, W. Yao, C.-Z. Chang, D. Cobden, D. Xiao, and X. Xu, Observation of fractionally quantized anomalous Hall effect, *Nature (London)* **622**, 74 (2023).
- [40] F. Xu, Z. Sun, T. Jia, C. Liu, C. Xu, C. Li, Y. Gu, K. Watanabe, T. Taniguchi, B. Tong, J. Jia, Z. Shi, S. Jiang, Y. Zhang, X. Liu, and T. Li, Observation of Integer and Fractional Quantum Anomalous Hall Effects in Twisted Bilayer MoTe₂, *Phys. Rev. X* **13**, 031037 (2023).
- [41] B. A. Foutty, C. R. Kometter, T. Devakul, A. P. Reddy, K. Watanabe, T. Taniguchi, L. Fu, and B. E. Feldman, Mapping twist-tuned multiband topology in bilayer WSe₂, *Science* **384**, 343 (2024).
- [42] K. Kang, B. Shen, Y. Qiu, Y. Zeng, Z. Xia, K. Watanabe, T. Taniguchi, J. Shan, and K. F. Mak, Evidence of the fractional quantum spin Hall effect in moiré MoTe₂, *Nature (London)* **628**, 522 (2024).
- [43] Y. Xia, Z. Han, K. Watanabe, T. Taniguchi, J. Shan, and K. F. Mak, Unconventional superconductivity in twisted bilayer WSe₂, arXiv:2405.14784 (2024).
- [44] Y. Guo, J. Pack, J. Swann, L. Holtzman, M. Cothrine, K. Watanabe, T. Taniguchi, D. Mandrus, K. Barmak, J. Hone, A. J. Millis, A. N. Pasupathy, C. R. Dean, Super-

- conductivity in twisted bilayer WSe₂, arXiv:2406.03418 (2024).
- [45] Y.-T. Hsu, F. Wu, and S. Das Sarma, Spin-valley locked instabilities in moiré transition metal dichalcogenides with conventional and higher-order Van Hove singularities, Phys. Rev. B **104**, 195134 (2021).
- [46] C. Schrade and L. Fu, Nematic, chiral and topological superconductivity in transition metal dichalcogenides, arXiv:2110.10172 (2021).
- [47] Y.-M. Wu, Z. Wu, and H. Yao, Pair-Density-Wave and Chiral Superconductivity in Twisted Bilayer Transition Metal Dichalcogenides, Phys. Rev. Lett. **130**, 126001 (2023).
- [48] S. Kim, J. F. Mendez-Valderrama, X. Wang, and D. Chowdhury, Theory of Correlated Insulator (s) and Superconductor at $\nu = 1$ in Twisted WSe₂, arXiv:2406.03525 (2024).
- [49] J. Zhu, Y.-Z. Chou, M. Xie, and S. D. Sarma, Theory of superconductivity in twisted transition metal dichalcogenide homobilayers, arXiv:2406.19348 (2024).
- [50] M. Christos, P. M. Bonetti, and M. S. Scheurer, Approximate symmetries, insulators, and superconductivity in continuum-model description of twisted WSe₂, arXiv:2407.02393 (2024).
- [51] C. S. Weber, D. Kiese, D. M. Kennes, and M. Claassen, Intertwined Superconductivity and Magnetism from Repulsive Interactions in Kondo Bilayers, arXiv:2408.02847 (2024).
- [52] C. Tuo, M.-R. Li, Z. Wu, W. Sun, and H. Yao, Theory of Topological Superconductivity and Antiferromagnetic Correlated Insulators in Twisted Bilayer WSe₂, arXiv:2409.06779 (2024).
- [53] T. Devakul, V. Crépel, Y. Zhang, and L. Fu, Magic in twisted transition metal dichalcogenide bilayers, Nat. Commun. **12**, 6730 (2021).
- [54] T. Cea and F. Guinea, Coulomb interaction, phonons, and superconductivity in twisted bilayer graphene, Proc. Natl. Acad. Sci. U.S.A. **118**, e2107874118 (2021).
- [55] A. Ghazaryan, T. Holder, M. Serbyn, and E. Berg, Unconventional Superconductivity in Systems with Annular Fermi Surfaces: Application to Rhombohedral Trilayer Graphene, Phys. Rev. Lett. **127**, 247001 (2021).
- [56] See supplemental information at xxxx.
- [57] Y. Jia, J. Yu, J. Liu, J. Herzog-Arbeitman, Z. Qi, H. Pi, N. Regnault, H. Weng, B. A. Bernevig, and Q. Wu, Moiré fractional Chern insulators. I. First-principles calculations and continuum models of twisted bilayer MoTe₂, Phys. Rev. B **109**, 205121 (2024).
- [58] W. Kohn and J. M. Luttinger, New Mechanism for Superconductivity, Phys. Rev. Lett. **15**, 524 (1965).
- [59] R. Nandkishore, L. S. Levitov, and A. V. Chubukov, Chiral superconductivity from repulsive interactions in doped graphene, Nat. Phys. **8**, 158 (2012).
- [60] W. Qin, C. Huang, T. Wolf, N. Wei, I. Blinov, and A. H. MacDonald, Functional Renormalization Group Study of Superconductivity in Rhombohedral Trilayer Graphene, Phys. Rev. Lett. **130**, 146001 (2023).
- [61] D. Guerci, D. Kaplan, J. Ingham, J. Pixley, and A. J. Millis, Topological superconductivity from repulsive interactions in twisted WSe₂, arXiv:2408.16075 (2024).

Supplemental Material for “Kohn-Luttinger Mechanism of Superconductivity in Twisted Bilayer WSe₂: Gate-Tunable Unconventional Pairing Symmetry”

Wei Qin,^{1,*} Wen-Xuan Qiu,² and Fengcheng Wu^{2,†}

¹*Department of Physics, University of Science and Technology of China, Hefei, Anhui 230026, China*

²*School of Physics and Technology, Wuhan University, Wuhan 430072, China*

(Dated: September 25, 2024)

I. CHARGE POLARIZATION FUNCTION

In the plane-wave basis, the static charge polarization function is expressed as

$$\Pi_{\mathbf{Q},\mathbf{Q}'}(\mathbf{q}) = \frac{1}{\beta A} \sum_{i\omega_n} \sum_{\tau\mathbf{k}} \sum_{\mathbf{G}\mathbf{G}'} \sum_{ll'} g_{l,\mathbf{G};l',\mathbf{G}'}^{\tau}(i\omega_n, \mathbf{k}) g_{l',\mathbf{G}'+\mathbf{Q}';l,\mathbf{G}+\mathbf{Q}}^{\tau}(i\omega_n, \mathbf{k} + \mathbf{q}), \quad (\text{S1})$$

where τ is the valley index, $\beta = 1/k_B T$, A denotes the area of the system, $\omega_n = (2n+1)\pi$ is the fermionic Matsubara frequency, l is the layer index, \mathbf{G} and \mathbf{Q} are morié reciprocal lattice vectors. By expanding the single-particle Green's function in the band representation, we have

$$g^{\tau}(i\omega_n, \mathbf{k}) = \sum_m \frac{|\tau m\mathbf{k}\rangle\langle\tau m\mathbf{k}|}{i\omega_n - \epsilon_{\tau m\mathbf{k}}} = \sum_m \frac{\rho_{\tau m\mathbf{k}}}{i\omega_n - \epsilon_{\tau m\mathbf{k}}}, \quad (\text{S2})$$

where $\epsilon_{\tau m\mathbf{k}}$ is the electron energy specified by valley τ , band m , and wavevector \mathbf{k} , and $\rho_{\tau m\mathbf{k}} = |\tau m\mathbf{k}\rangle\langle\tau m\mathbf{k}|$ denotes the density matrix defined by the state $|\tau m\mathbf{k}\rangle$. By substituting Eq. (S2) into Eq. (S1),

$$\begin{aligned} \Pi_{\mathbf{Q},\mathbf{Q}'}(\mathbf{q}) &= \frac{1}{\beta A} \sum_{i\omega_n} \sum_{\mathbf{k}} \sum_{\mathbf{G}\mathbf{G}'} \sum_{ll'} \sum_{mm'} \frac{[\rho_{m\mathbf{k}}]_{l,\mathbf{G};l',\mathbf{G}'}}{i\omega_n - \epsilon_{m\mathbf{k}}} \frac{[\rho_{m'\mathbf{k}+\mathbf{q}}]_{l',\mathbf{G}'+\mathbf{Q}';l,\mathbf{G}+\mathbf{Q}}}{i\omega_n - \epsilon_{m'\mathbf{k}+\mathbf{q}}} \\ &= \frac{1}{A} \sum_{mm'\mathbf{k}} \frac{f(\epsilon_{m\mathbf{k}}) - f(\epsilon_{m'\mathbf{k}+\mathbf{q}})}{\epsilon_{m\mathbf{k}} - \epsilon_{m'\mathbf{k}+\mathbf{q}}} \sum_{ll'\mathbf{G}\mathbf{G}'} [\rho_{m\mathbf{k}}]_{l,\mathbf{G};l',\mathbf{G}'} [\rho_{m'\mathbf{k}+\mathbf{q}}]_{l',\mathbf{G}'+\mathbf{Q}';l,\mathbf{G}+\mathbf{Q}}, \end{aligned} \quad (\text{S3})$$

recovering Eq. (5) in the main text. In Eq. (S3), the valley index is omitted for simplification. The valley-specific $\Pi^{\tau}(\mathbf{q})$ is obtained by directly replacing the electron energies and density matrices in Eq. (S3) with their valley-specific forms.

Here we demonstrate that $\Pi(\mathbf{q})$ possesses several properties. First, from Eq. (S3), we have

$$\begin{aligned} \Pi_{\mathbf{Q}',\mathbf{Q}}^{*}(\mathbf{q}) &= \frac{1}{A} \sum_{mm'\mathbf{k}} \frac{f(\epsilon_{m\mathbf{k}}) - f(\epsilon_{m'\mathbf{k}+\mathbf{q}})}{\epsilon_{m\mathbf{k}} - \epsilon_{m'\mathbf{k}+\mathbf{q}}} \sum_{ll'\mathbf{G}\mathbf{G}'} [\rho_{m\mathbf{k}}]_{l,\mathbf{G};l',\mathbf{G}'}^{*} [\rho_{m'\mathbf{k}+\mathbf{q}}]_{l',\mathbf{G}'+\mathbf{Q};l,\mathbf{G}+\mathbf{Q}'}^{*} \\ &= \frac{1}{A} \sum_{mm'\mathbf{k}} \frac{f(\epsilon_{m\mathbf{k}}) - f(\epsilon_{m'\mathbf{k}+\mathbf{q}})}{\epsilon_{m\mathbf{k}} - \epsilon_{m'\mathbf{k}+\mathbf{q}}} \sum_{ll'\mathbf{G}\mathbf{G}'} [\rho_{m\mathbf{k}}]_{l',\mathbf{G}';l,\mathbf{G}} [\rho_{m'\mathbf{k}+\mathbf{q}}]_{l,\mathbf{G}+\mathbf{Q}';l',\mathbf{G}'+\mathbf{Q}}, \\ &= \Pi_{\mathbf{Q},\mathbf{Q}'}(\mathbf{q}) \end{aligned} \quad (\text{S4})$$

where the relation $\rho_{m\mathbf{k}} = \rho_{m\mathbf{k}}^{\dagger}$ is employed. The above equation implies $\Pi(\mathbf{q}) = \Pi^{\dagger}(\mathbf{q})$ is a Hermitian matrix. Secondly,

*Electronic address: qinwei5@ustc.edu.cn

†Electronic address: wufcheng@whu.edu.cn

we have

$$\begin{aligned}
\Pi_{-\mathbf{Q}', -\mathbf{Q}}(-\mathbf{q}) &= \frac{1}{A} \sum_{mm'\mathbf{k}} \frac{f(\epsilon_{m\mathbf{k}}) - f(\epsilon_{m'\mathbf{k}-\mathbf{q}})}{\epsilon_{m\mathbf{k}} - \epsilon_{m'\mathbf{k}-\mathbf{q}}} \sum_{ll'\mathbf{G}\mathbf{G}'} [\rho_{m\mathbf{k}}]_{l,\mathbf{G};l',\mathbf{G}'} [\rho_{m'\mathbf{k}-\mathbf{q}}]_{l',\mathbf{G}'-\mathbf{Q};l,\mathbf{G}-\mathbf{Q}'} \\
&= \frac{1}{A} \sum_{mm'\mathbf{k}} \frac{f(\epsilon_{m\mathbf{k}+\mathbf{q}}) - f(\epsilon_{m'\mathbf{k}})}{\epsilon_{m\mathbf{k}+\mathbf{q}} - \epsilon_{m'\mathbf{k}}} \sum_{ll'\mathbf{G}\mathbf{G}'} [\rho_{m\mathbf{k}+\mathbf{q}}]_{l,\mathbf{G};l',\mathbf{G}'} [\rho_{m'\mathbf{k}}]_{l',\mathbf{G}'-\mathbf{Q};l,\mathbf{G}-\mathbf{Q}'} \\
&= \frac{1}{A} \sum_{mm'\mathbf{k}} \frac{f(\epsilon_{m'\mathbf{k}+\mathbf{q}}) - f(\epsilon_{m\mathbf{k}})}{\epsilon_{m'\mathbf{k}+\mathbf{q}} - \epsilon_{m\mathbf{k}}} \sum_{ll'\mathbf{G}\mathbf{G}'} [\rho_{m'\mathbf{k}+\mathbf{q}}]_{l,\mathbf{G}'+\mathbf{Q}';l',\mathbf{G}+\mathbf{Q}} [\rho_{m\mathbf{k}}]_{l',\mathbf{G};l,\mathbf{G}'} \\
&= \Pi_{\mathbf{Q}, \mathbf{Q}'}(\mathbf{q}),
\end{aligned} \tag{S5}$$

indicating the inversion symmetry $\Pi_{\mathbf{Q}, \mathbf{Q}'}(\mathbf{q}) = \Pi_{-\mathbf{Q}', -\mathbf{Q}}(-\mathbf{q})$. Thirdly, it is straightforward to demonstrate that $\Pi_{\mathbf{Q}, \mathbf{Q}'}(\mathbf{q}) = \Pi_{\hat{C}_3\mathbf{Q}, \hat{C}_3\mathbf{Q}'}(\hat{C}_3\mathbf{q})$ by recognizing that the system preserves three-fold rotational symmetry, which requires $\epsilon_{m\mathbf{k}} = \epsilon_{m\hat{C}_3\mathbf{k}}$ and $[\rho_{m\mathbf{k}}]_{l,\mathbf{G};l',\mathbf{G}'} = [\rho_{m\hat{C}_3\mathbf{k}}]_{l,\hat{C}_3\mathbf{G};l',\hat{C}_3\mathbf{G}'}$. Finally, time-reversal symmetry imposes the relations

$$\begin{aligned}
\epsilon_{Km,\mathbf{k}} &= \epsilon_{K'm,-\mathbf{k}}, \\
[\rho_{Km,\mathbf{k}}]_{l,\mathbf{G};l',\mathbf{G}'} &= [\rho_{K'm,-\mathbf{k}}]_{l,-\mathbf{G};l',-\mathbf{G}'}^*.
\end{aligned} \tag{S6}$$

Therefore, we have

$$\begin{aligned}
\Pi_{\mathbf{Q}, \mathbf{Q}'}^K(\mathbf{q}) &= \frac{1}{A} \sum_{mm'\mathbf{k}} \frac{f(\epsilon_{Km,\mathbf{k}}) - f(\epsilon_{K'm',\mathbf{k}+\mathbf{q}})}{\epsilon_{Km,\mathbf{k}} - \epsilon_{K'm',\mathbf{k}+\mathbf{q}}} \sum_{ll'\mathbf{G}\mathbf{G}'} [\rho_{Km,\mathbf{k}}]_{l,\mathbf{G};l',\mathbf{G}'} [\rho_{Km',\mathbf{k}+\mathbf{q}}]_{l',\mathbf{G}'+\mathbf{Q}';l,\mathbf{G}+\mathbf{Q}} \\
&= \frac{1}{A} \sum_{mm'\mathbf{k}} \frac{f(\epsilon_{K'm,-\mathbf{k}}) - f(\epsilon_{K'm',-\mathbf{k}-\mathbf{q}})}{\epsilon_{K'm,-\mathbf{k}} - \epsilon_{K'm',-\mathbf{k}-\mathbf{q}}} \sum_{ll'\mathbf{G}\mathbf{G}'} [\rho_{K'm,-\mathbf{k}}]_{l,-\mathbf{G};l',-\mathbf{G}'}^* [\rho_{K'm',-\mathbf{k}-\mathbf{q}}]_{l',-\mathbf{G}'-\mathbf{Q}';l,-\mathbf{G}-\mathbf{Q}} \\
&= \frac{1}{A} \sum_{mm'\mathbf{k}} \frac{f(\epsilon_{K'm,\mathbf{k}}) - f(\epsilon_{K'm',\mathbf{k}-\mathbf{q}})}{\epsilon_{K'm,\mathbf{k}} - \epsilon_{K'm',\mathbf{k}-\mathbf{q}}} \sum_{ll'\mathbf{G}\mathbf{G}'} [\rho_{K'm,\mathbf{k}}]_{l,\mathbf{G};l',\mathbf{G}'}^* [\rho_{K'm',\mathbf{k}-\mathbf{q}}]_{l',\mathbf{G}'-\mathbf{Q}';l,\mathbf{G}-\mathbf{Q}} \\
&= [\Pi_{-\mathbf{Q}, -\mathbf{Q}'}^{K'}(-\mathbf{q})]^*.
\end{aligned} \tag{S7}$$

These properties of $\Pi(\mathbf{q})$ are summarized as follows:

$$\begin{aligned}
\Pi_{\mathbf{Q}, \mathbf{Q}'}(\mathbf{q}) &= \Pi_{\mathbf{Q}', \mathbf{Q}}^*(\mathbf{q}), \\
\Pi_{\mathbf{Q}, \mathbf{Q}'}(\mathbf{q}) &= \Pi_{-\mathbf{Q}', -\mathbf{Q}}(-\mathbf{q}), \\
\Pi_{\mathbf{Q}, \mathbf{Q}'}(\mathbf{q}) &= \Pi_{\hat{C}_3\mathbf{Q}, \hat{C}_3\mathbf{Q}'}(\hat{C}_3\mathbf{q}), \\
\Pi_{\mathbf{Q}, \mathbf{Q}'}^K(\mathbf{q}) &= [\Pi_{-\mathbf{Q}, -\mathbf{Q}'}^{K'}(-\mathbf{q})]^*.
\end{aligned} \tag{S8}$$

Based on these relations, we have $\Pi_{\mathbf{Q}, \mathbf{Q}'}^K(\mathbf{q}) = \Pi_{\mathbf{Q}, \mathbf{Q}'}^{K'}(\mathbf{q})$, suggesting the charge polarization function is valley-independent. Since the bare Coulomb potential $V_0(\mathbf{q})$ naturally satisfies these relations, it can be readily demonstrated that the screened Coulomb potential $V_{\mathbf{Q}, \mathbf{Q}'}^s(\mathbf{q})$, derived from Eq. (4) in the main text, also satisfies the relations summarized in Eq. (S8).

II. SCREENED COULOMB INTERACTION

Within the random phase approximation, the reciprocal-space screened Coulomb potential $V_{\mathbf{Q}, \mathbf{Q}'}^s(\mathbf{q})$ is given by Eq. (4) in the main text. Hence, the real-space effective interaction between two electrons (holes) located at \mathbf{r} and \mathbf{r}' is obtained by performing the following Fourier's transformation

$$\begin{aligned}
V(\mathbf{r}, \mathbf{r}') &= \frac{1}{A} \sum_{\mathbf{Q}\mathbf{Q}'} \sum_{\mathbf{q}} V_{\mathbf{Q}, \mathbf{Q}'}^s(\mathbf{q}) e^{i(\mathbf{q}+\mathbf{Q}) \cdot \mathbf{r} - i(\mathbf{q}+\mathbf{Q}') \cdot \mathbf{r}'} \\
&= \frac{1}{A} \sum_{\mathbf{Q}\mathbf{Q}'} \sum_{\mathbf{q}} V_{\mathbf{Q}, \mathbf{Q}'}^s(\mathbf{q}) e^{i(\mathbf{q}+\mathbf{Q}) \cdot (\mathbf{r}-\mathbf{r}') + i(\mathbf{Q}-\mathbf{Q}') \cdot \mathbf{r}'},
\end{aligned} \tag{S9}$$

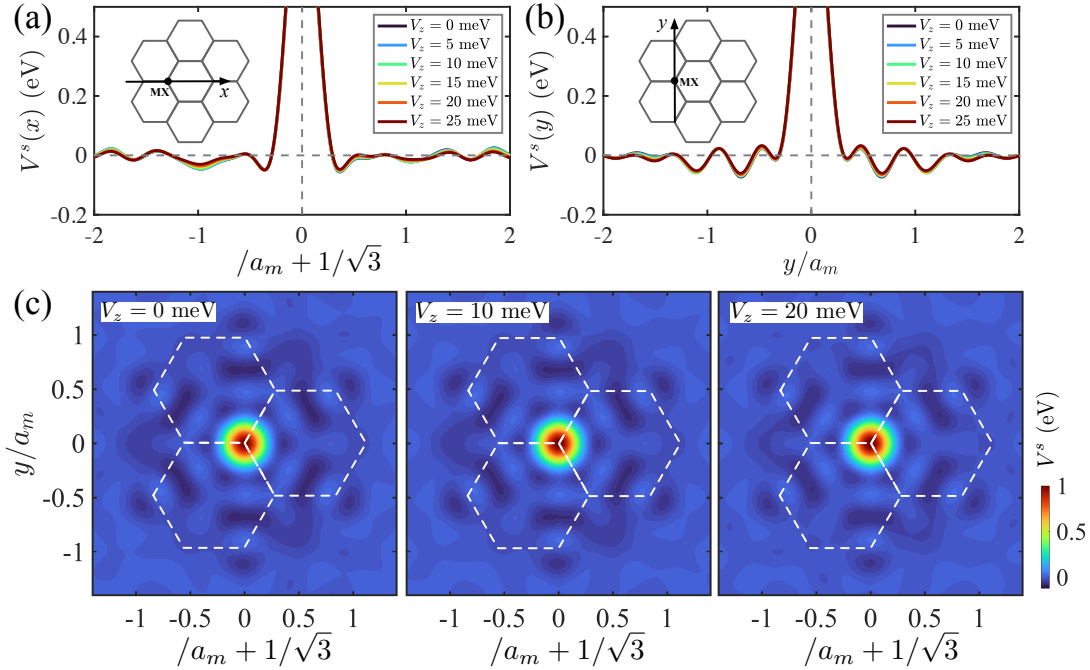


FIG. S1: Real-space structures of screened Coulomb potential V^s measured from the MX stacking center: (a)-(b) V^s plotted along (a) x and (b) y directions, as defined in the insets. (c) Two-dimensional color plots of $V^s(\mathbf{r})$ for three typical values of V_z , where the dashed hexagons indicate the morié supercells. These calculations are performed at the van Hove fillings for given values of V_z , with temperature $T = 50$ mK.

where the off-diagonal terms of $V_{\mathbf{Q},\mathbf{Q}'}^s(\mathbf{q})$ with $\mathbf{Q} \neq \mathbf{Q}'$ break the translational symmetry within the morié period. By setting the origin of the coordinate system at the MM stacking center, we have

$$V(\mathbf{r}, 0) = \frac{1}{A} \sum_{\mathbf{Q}\mathbf{q}} e^{i(\mathbf{q}+\mathbf{Q}) \cdot \mathbf{r}} \sum_{\mathbf{Q}'} V_{\mathbf{Q},\mathbf{Q}'}^s(\mathbf{q}). \quad (\text{S10})$$

The corresponding results for several typical values of layer potential V_z are shown in Fig. 2 in the main text.

Figures S1 and S2 show the results obtained by choosing MX and XM stacking centers as the origins of the coordinate system, respectively. These calculations are performed by setting $\mathbf{r}' = (\mp a_m/\sqrt{3}, 0)$ in Eq. (S9), where $a_m = a_0/\theta$ denotes the morié period with θ being the twist angle. Similar to the case of MM stacking, $V^s(\mathbf{r})$ for both cases of MX and XM exhibit significant reductions around the morié length scale, and develops attractive regimes along the directions of morié lattice vectors. However, unlike the case of MM, where $V^s(\mathbf{r})$ possesses six-fold rotational symmetry for $V_z = 0$ meV, $V^s(\mathbf{r})$ for the cases of MX and XM exhibits three-fold rotational symmetry, as illustrated in Fig. S1(c) and Fig. S2(c). This is because the lattice symmetry is reduced with respect to the MX and XM stacking centers.

III. LINEARIZED GAP EQUATION

In the plane-wave basis, the linearized gap equation depicted in Fig. 3(a) of the main text is interpreted as

$$\begin{aligned} \Delta_{l\mathbf{G};l'\mathbf{G}'}(\mathbf{k}) &= - \sum_{\mathbf{QQ}'\mathbf{k}'} V_{\mathbf{Q},\mathbf{Q}'}^s(\mathbf{k} - \mathbf{k}') \sum_{i\omega_n} \sum_{l_1 l'_1} \sum_{\mathbf{G}_1 \mathbf{G}'_1} \mathcal{G}_{l_1, \mathbf{G}_1; l, \mathbf{G} - \mathbf{Q}}^K(i\omega_n, \mathbf{k}') \mathcal{G}_{l'_1, \mathbf{G}'_1; l', \mathbf{G}' + \mathbf{Q}'}^{K'}(-i\omega_n, -\mathbf{k}') \Delta_{l_1, \mathbf{G}_1; l'_1, \mathbf{G}'_1}(\mathbf{k}') \\ &= - \sum_{mm'k'} \frac{f(\epsilon_{Km\mathbf{k}'}) - f(-\epsilon_{Km'\mathbf{k}'})}{\epsilon_{Km\mathbf{k}'} + \epsilon_{Km'\mathbf{k}'}} \sum_{\mathbf{QQ}'} V_{\mathbf{Q},\mathbf{Q}'}^s(\mathbf{k} - \mathbf{k}') [\rho_{Km\mathbf{k}'}]_{l_1, \mathbf{G}_1; l, \mathbf{G} - \mathbf{Q}} [\rho_{Km'\mathbf{k}'}]_{l'_1, -\mathbf{G}'_1; l', -\mathbf{G}' - \mathbf{Q}'} \Delta_{l_1 \mathbf{G}_1; l'_1 \mathbf{G}'_1}(\mathbf{k}'), \end{aligned} \quad (\text{S11})$$

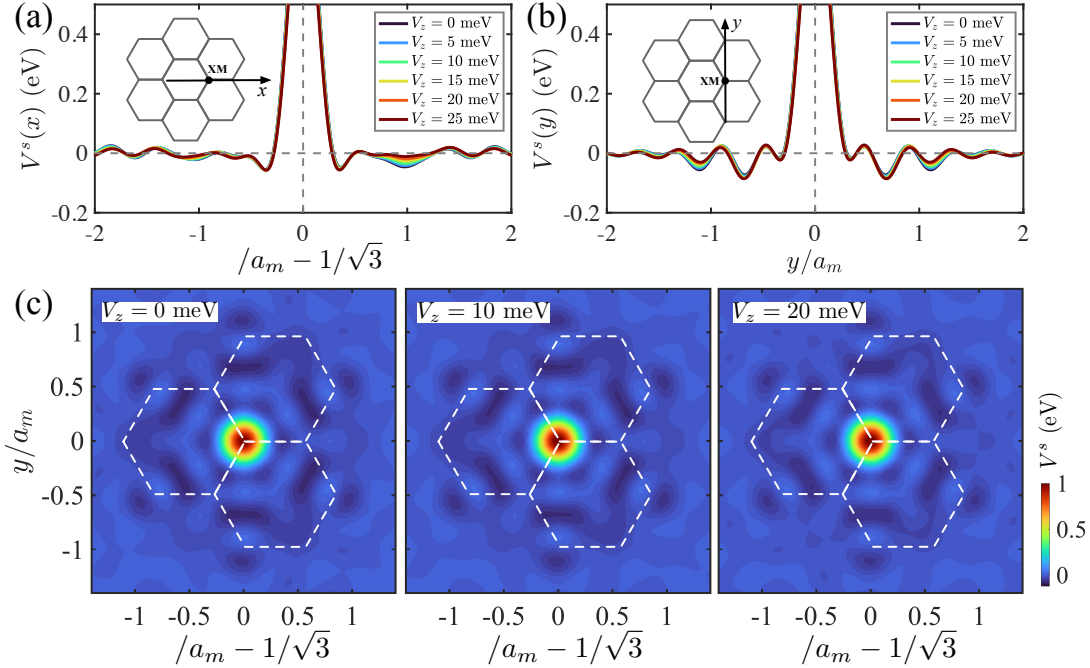


FIG. S2: Real-space structures of screened Coulomb potential V^s measured from the XM stacking center: (a)-(b) V^s plotted along (a) x and (b) y directions, as defined in the insets. (c) Two-dimensional color plots of $V^s(\mathbf{r})$ for three typical values of V_z , where the dashed hexagons indicate the morié supercells. These calculations are performed at the van Hove fillings for given values of V_z , with temperature $T = 50$ mK.

where the relation provided in Eq. (S6) is employed. At low temperatures, the above equation is predominantly contributed by the first moiré band. Therefore, we apply the single-band approximation and have

$$\Delta_{l\mathbf{G};l'\mathbf{G}'}(\mathbf{k}) = - \sum_{\mathbf{k}'} \frac{\tanh(\beta\epsilon_{\mathbf{k}'}/2)}{2\epsilon_{\mathbf{k}'}} \sum_{\mathbf{Q}\mathbf{Q}'} V_{\mathbf{Q},\mathbf{Q}'}^s(\mathbf{k} - \mathbf{k}') [\rho_{\mathbf{k}'}]_{l_1,\mathbf{G}_1;l,\mathbf{G}-\mathbf{Q}} [\rho_{\mathbf{k}'}]_{l'_1,-\mathbf{G}'_1;l',-\mathbf{G}'-\mathbf{Q}'} \Delta_{l_1\mathbf{G}_1;l'_1\mathbf{G}'_1}(\mathbf{k}'), \quad (\text{S12})$$

where $\epsilon_{\mathbf{k}'}$ and $\rho_{\mathbf{k}'}$ denote the electron energy and density matrix of the K -valley first morié band, respectively. Within the band representation, we have

$$\Delta_{\mathbf{k}} = \sum_{l'\mathbf{G}\mathbf{G}'} [\rho_{\mathbf{k}}]_{l,\mathbf{G};l',-\mathbf{G}'} \Delta_{l\mathbf{G};l'\mathbf{G}'}(\mathbf{k}), \quad (\text{S13})$$

where $\Delta_{\mathbf{k}}$ denotes the superconducting order parameter projected onto the first morié band. By substituting Eq. (S13) into Eq. (S12), we reach Eq. (6) of the main text, namely,

$$\Delta_{\mathbf{k}} = - \sum_{\mathbf{k}'} V_b^s(\mathbf{k}, \mathbf{k}') \frac{\tanh(\beta\epsilon_{\mathbf{k}'}/2)}{2\epsilon_{\mathbf{k}'}} \Delta_{\mathbf{k}'}, \quad (\text{S14})$$

where

$$V_b^s(\mathbf{k}, \mathbf{k}') = \sum_{\mathbf{Q}\mathbf{Q}'} \sum_{ll'\mathbf{G}\mathbf{G}'} [\rho_{\mathbf{k}}]_{l,\mathbf{G};l',\mathbf{G}'} V_{\mathbf{Q},\mathbf{Q}'}^s(\mathbf{k} - \mathbf{k}') [\rho_{\mathbf{k}'}]_{l',\mathbf{G}'-\mathbf{Q}';l,\mathbf{G}-\mathbf{Q}}, \quad (\text{S15})$$

representing the first morié band-projected screened Coulomb potential.

Figure S3 presents the results of $V_b^s(\mathbf{k}, \mathbf{k}')$ by setting \mathbf{k}' at the γ point of the morié Brillouin zone. In contrast to the real-space structures of $V^s(\mathbf{r})$, which remain nearly unaffected upon increasing V_z , the k -space structure of $V_b^s(\mathbf{k}, \mathbf{k}')$ shows a significant dependence on V_z , as illustrated in Fig. S3. Based on Eq. (S15), we note that the changes in $V_b^s(\mathbf{k}, \mathbf{k}')$ arise mainly from the wave function effect imprinted in the density matrix $\rho_{\mathbf{k}}$, as the band structure undergoes significant changes with increasing V_z .

In the main text, we primarily present the results for $\theta = 5^\circ$. We have also preformed calculations for $\theta = 3.65^\circ$ and

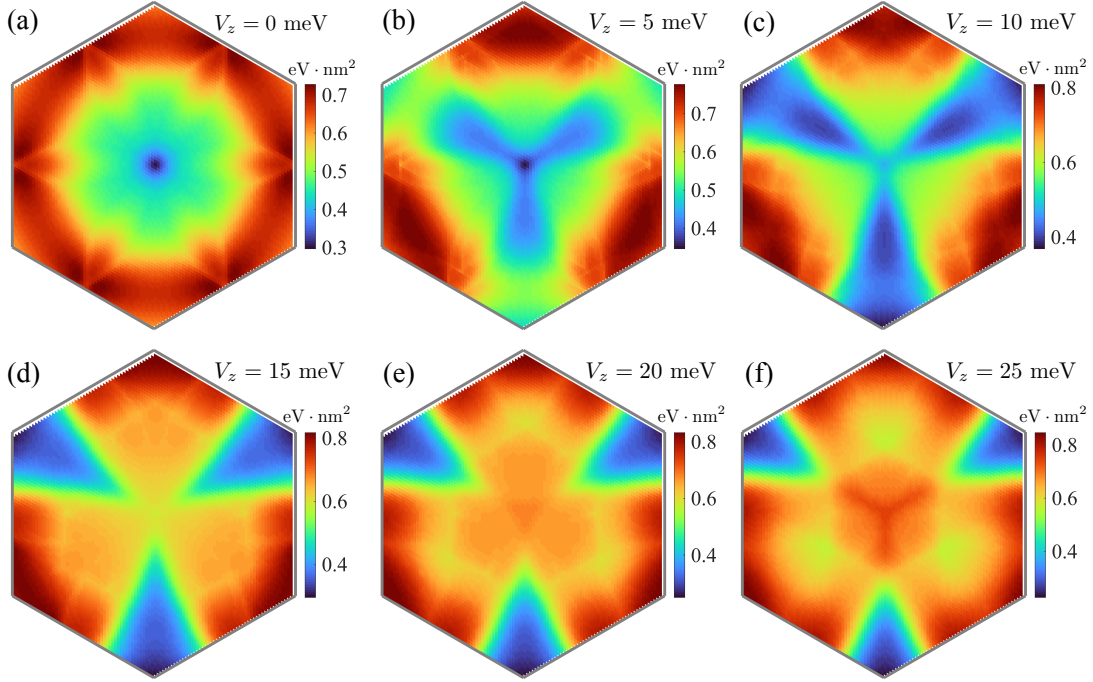


FIG. S3: (a)-(f) The first morié band-projected screened Coulomb potential $V_b^s(\mathbf{k}, 0)$ for different values of V_z . These results are obtained at the van Hove fillings by choosing twist angle $\theta = 5^\circ$, dielectric constant $\epsilon = 5$, gate-sample distance $d_s = 11$ nm, and temperature $T = 50$ mK.

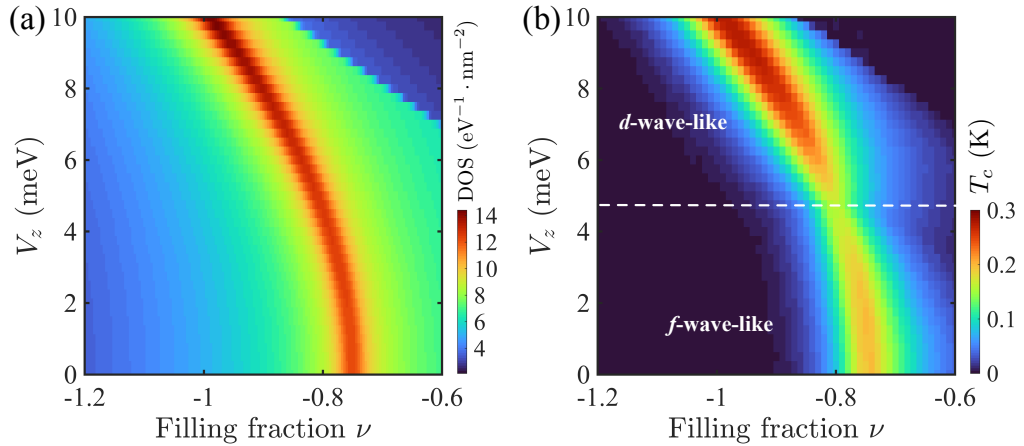


FIG. S4: (a)-(b) Two-dimensional maps of (a) the density of states (DOS) and (b) the critical temperature T_c as functions of filling fraction ν and V_z for tWSe₂ with twist angle $\theta = 3.65^\circ$. The horizontal dashed line in (b) indicates the phase boundary between f -wave-like and doubly degenerate d -wave-like pairing states.

found similar results. As shown in Fig. S4(a), the density of states (DOS) at van Hove filling increases monotonously with increasing V_z for $\theta = 3.65^\circ$. For given values of V_z , T_c maxima occur at the corresponding van Hove singularities. Similar to the case of $\theta = 5^\circ$, T_c^{VHS} does not follow the trend of DOS and exhibits a non-monotonic behavior. As V_z increases from 0 meV, T_c^{VHS} initially rise to a maximum at $V_z \approx 1.5$ meV, subsequently decreases to a minimum at $V_z \approx 4.5$ meV, and then increases again. Similarly, we find a phase transition from f -wave-like pairing state to doubly degenerate d -wave-like pairing state upon increasing V_z .

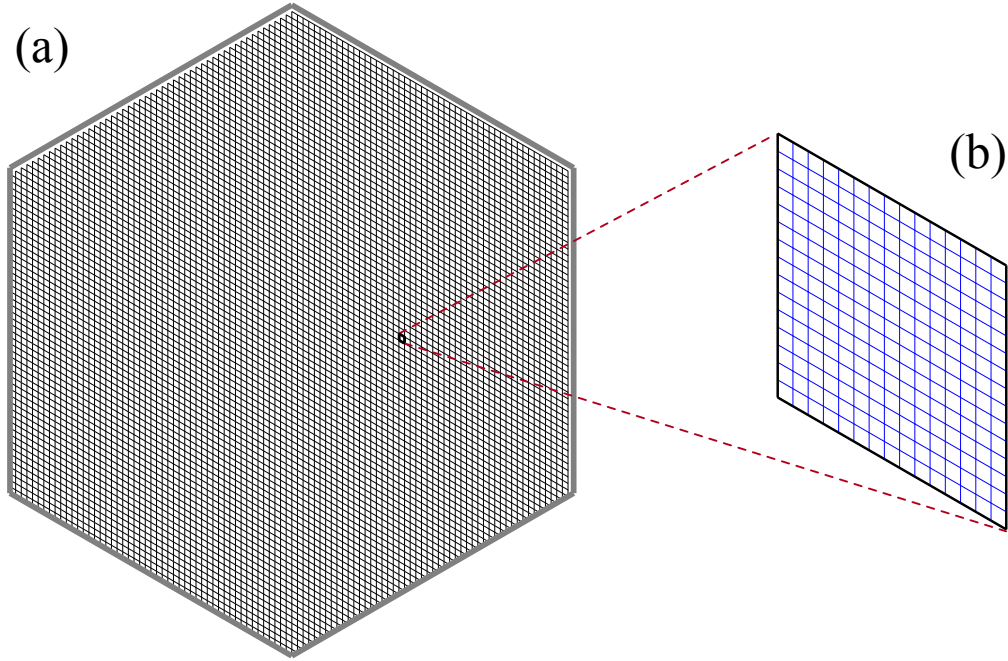


FIG. S5: Two-step discretization of the MBZ (hexagon). (a) The MBZ is divided into $N = 7500$ meshes to provide a smooth description of the wave function effect. (b) Each mesh from (a) is further subdivided into $N_1 = 225$ submeshes to enable an accurate calculation of the band effect, which is more sensitive to the Fermi surface.

IV. NUMERICAL DETAILS

In this section, we provide the numerical details employed to obtain the results presented in the preceding sections and the main text. As indicated by the right-hand side of Eq. (S3), the charge polarization function $\Pi_{\mathbf{Q},\mathbf{Q}'}(\mathbf{q})$ is affected by two factors: the band effect and wave function effect (form factors), characterized by $[f(\epsilon_{m\mathbf{k}}) - f(\epsilon_{m'\mathbf{k}+\delta\mathbf{k}})]/(\epsilon_{m\mathbf{k}} - \epsilon_{m'\mathbf{k}+\delta\mathbf{k}})$ and density matrix $\rho_{m\mathbf{k}}$, respectively. The former is sensitive to changes in the Fermi surface, whereas the latter is less sensitive. Therefore, to ensure both the accuracy and efficiency of the numerical computations, we employ a two-step discretization of the moiré Brillouin zone (MBZ), as schematically illustrated in Fig. S5. Specifically, the first step divides the MBZ into $N = 7500$ meshes, as illustrated in Fig. S5(a), to capture the effects induced by wave function. The second step further refines each mesh into $N_1 = 225$ sub meshes, as shown in Fig. S5(b), to allow for a more accurate calculation of the band effect. Within this two-step scheme, Eq. (S3) is represented as

$$\Pi_{\mathbf{Q},\mathbf{Q}'}(\mathbf{q}) = \frac{1}{A} \sum_{mm'\mathbf{k} \in N} \frac{1}{N_1} \sum_{\delta\mathbf{k} \in N_1} \frac{f(\epsilon_{m\mathbf{k}+\delta\mathbf{k}}) - f(\epsilon_{m'\mathbf{k}+\delta\mathbf{k}+\delta\mathbf{q}})}{\epsilon_{m\mathbf{k}+\delta\mathbf{k}} - \epsilon_{m'\mathbf{k}+\delta\mathbf{k}+\delta\mathbf{q}}} \sum_{ll'GG'} [\rho_{m\mathbf{k}}]_{l,\mathbf{G};l',\mathbf{G}'} [\rho_{m'\mathbf{k}+\delta\mathbf{k}}]_{l',\mathbf{G}'+\mathbf{Q}';l,\mathbf{G}+\mathbf{Q}}, \quad (\text{S16})$$

where \mathbf{k} denotes the center-of-mesh wavevector shown in Fig. S5(a), and $\delta\mathbf{k}$ is measured from \mathbf{k} , representing the wavevector of the submeshes depicted in Fig. S5(b).

Figure S6 shows an example of $\Pi_{\mathbf{Q},\mathbf{Q}'}(\mathbf{q})$, specifically focusing on the diagonal terms, calculated at the van Hove singularity (VHS) for $V_z = 0$ meV. The dominant contribution arises from $\Pi_{0,0}(\mathbf{q})$, as depicted in the center hexagon of the left panel of Fig. S6. Six satellite domains are observed in the third-shell MBZs ($\Pi_{\mathbf{Q}_3,\mathbf{Q}_3}(\mathbf{q})$). As enlarged in the right panel of Fig. S6, contributions from the fourth-shell ($\Pi_{\mathbf{Q}_4,\mathbf{Q}_4}(\mathbf{q})$) and fifth-shell ($\Pi_{\mathbf{Q}_5,\mathbf{Q}_5}(\mathbf{q})$) to $\Pi_{\mathbf{Q},\mathbf{Q}'}(\mathbf{q})$ become negligible. Therefore, in this work, we truncate our numerical calculations of charge polarization function to include contributions up to the third-shell morié reciprocal lattice vectors.

As illustrated in Fig. S3, the first morié band-projected screened Coulomb potential $V_b^s(\mathbf{k}, \mathbf{k}')$ varies slowly within the MBZ, indicating that a less dense \mathbf{k} -mesh (e.g. $N = 7500$ in this work) is sufficient to capture its variation. In contrast, the particle-particle channel susceptibility $\tanh(\beta\epsilon_{\mathbf{k}'}/2)/2\epsilon_{\mathbf{k}'}$ typically exhibits a logarithmic divergence behavior at low temperatures, requiring a denser \mathbf{k} -mesh to accurately capture its low-temperature behavior. Therefore, we adopt a similar two-step discretization of the MBZ, as depicted in Fig. S5, in solving the linearized gap equation. Within

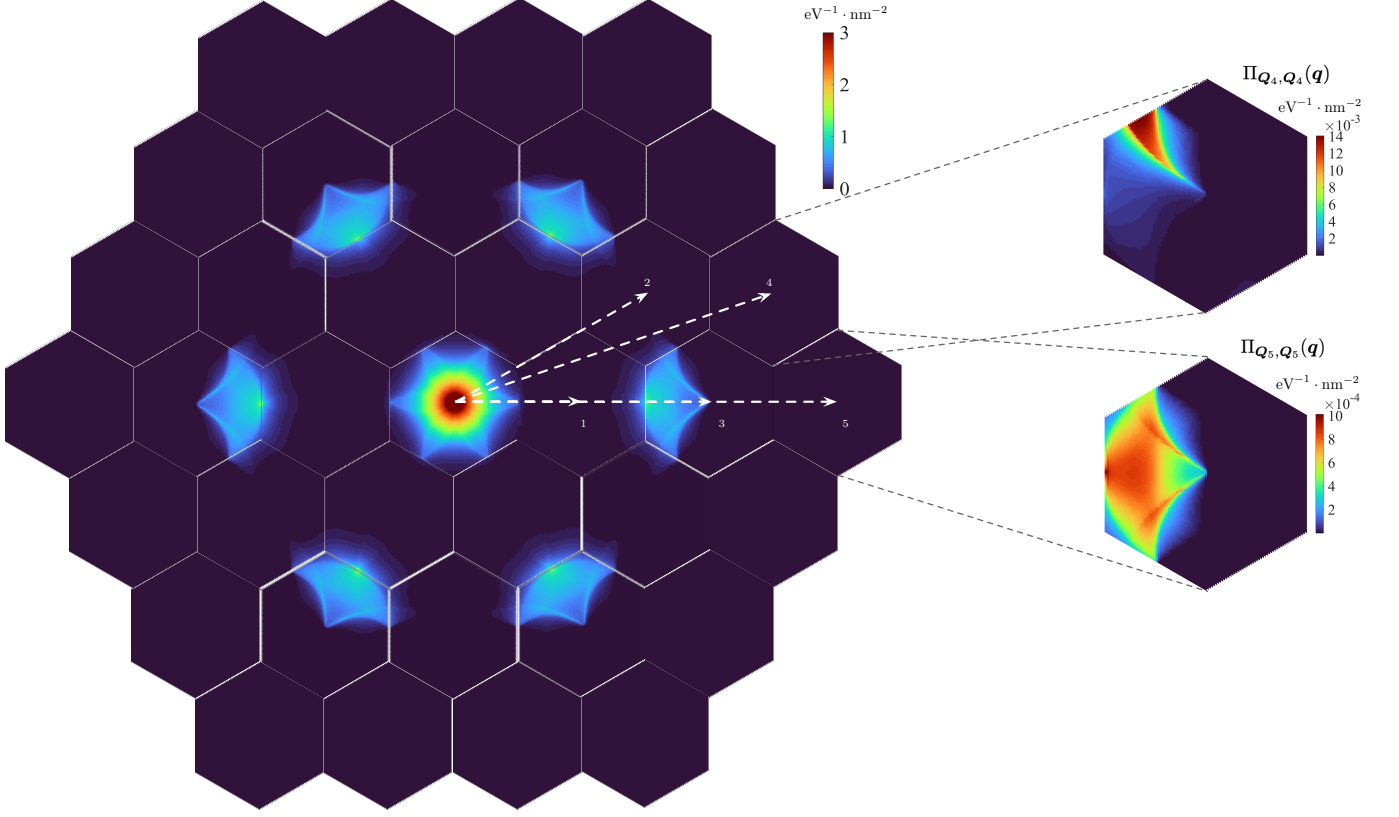


FIG. S6: Two-dimensional maps of the diagonal terms $\Pi_{\mathbf{Q},\mathbf{Q}}(\mathbf{q})$ of the charge polarization function. Left panel shows $\Pi_{\mathbf{Q},\mathbf{Q}}(\mathbf{q})$ up to fifth reciprocal lattice vector \mathbf{Q}_5 , as defined by the dashed arrows. Right panel shows the enlarged results of the fourth-shell (top) and fifth-shell (bottom) contributions to $\Pi_{\mathbf{Q},\mathbf{Q}}(\mathbf{q})$. These results are obtained at the VHS for $\theta = 5^\circ$ and $V_z = 0$ meV.

this framework, Eq. (S14) is expressed as

$$\Delta_{\mathbf{k}} = - \sum_{\mathbf{k}' \in N} V_b^s(\mathbf{k}, \mathbf{k}') \Delta_{\mathbf{k}'} \frac{1}{N_1} \sum_{\delta \mathbf{k} \in N_1} \frac{\tanh(\beta \epsilon_{\mathbf{k}'+\delta \mathbf{k}}/2)}{2\epsilon_{\mathbf{k}'+\delta \mathbf{k}}}. \quad (\text{S17})$$

As demonstrated in Figs. 3 and 5 in the main text, this "two-step" scheme yields smooth variations of the superconducting critical temperature T_c to within a few milliKelvins upon changing the filling factors and displacement fields.